

Measuring Topological Invariants in a Polaritonic Analog of Graphene


P. St-Jean,¹ A. Dauphin², P. Massignan^{2,3}, B. Real,⁴ O. Jamadi,⁴ M. Milicevic,¹ A. Lemaître,¹
A. Harouri,¹ L. Le Gratiet,¹ I. Sagnes,¹ S. Ravets,¹ J. Bloch,¹ and A. Amo⁴

¹Centre de Nanosciences et de Nanotechnologies (C2N), CNRS—Université Paris-Sud/Paris-Saclay, Palaiseau 91120, France

²ICFO-Institut de Ciències Fòniques, The Barcelona Institute of Science and Technology,
Avinguda Carl Friedrich Gauss 3, 08860 Castelldefels (Barcelona), Spain

³Departament de Física, Universitat Politècnica de Catalunya, Campus Nord B4-B5, 08034 Barcelona, Spain

⁴Univ. Lille, CNRS, UMR 8523—PhLAM—Physique des Lasers Atomes et Molécules, F-59000 Lille, France

 (Received 23 June 2020; revised 8 September 2020; accepted 3 February 2021; published 25 March 2021)

Topological materials rely on engineering global properties of their bulk energy bands called topological invariants. These invariants, usually defined over the entire Brillouin zone, are related to the existence of protected edge states. However, for an important class of Hamiltonians corresponding to 2D lattices with time-reversal and chiral symmetry (e.g., graphene), the existence of edge states is linked to invariants that are not defined over the full 2D Brillouin zone, but on reduced 1D subspaces. Here, we demonstrate a novel scheme based on a combined real- and momentum-space measurement to directly access these 1D topological invariants in lattices of semiconductor microcavities confining exciton polaritons. We extract these invariants in arrays emulating the physics of regular and critically compressed graphene where Dirac cones have merged. Our scheme provides a direct evidence of the bulk-edge correspondence in these systems and opens the door to the exploration of more complex topological effects, e.g., involving disorder and interactions.

DOI: [10.1103/PhysRevLett.126.127403](https://doi.org/10.1103/PhysRevLett.126.127403)

Topological bands are characterized by integer-valued quantities, called topological invariants, that are typically defined as the integral of a local property (e.g., the Berry curvature) over the full Brillouin zone (BZ). The hallmark of these invariants is their robustness against local perturbations, which endows topological matter with properties that are insensitive to certain types of disorder [1,2]. One notable example is provided by the edge conductivity plateaus in the quantum Hall effect that can be linked to a topological invariant called the Chern number [3].

A distinct situation arises in 2D crystals presenting time-reversal and chiral (or sublattice) symmetry, such as honeycomb, Lieb, or Mielke lattices. The bands of these materials are either ungapped or present a globally vanishing Berry curvature; they thus cannot be described by a nonzero first-order topological invariant defined over the entire BZ such as the Chern number. Yet, for well-defined crystalline terminations, these materials present edge states that can be linked to topological invariants defined over reduced (1D) subspaces of the BZ [4,5].

So far, these 1D invariants have solely been determined indirectly by probing the emergence of edge states in honeycomb lattices [6,7]. Yet, they are bulk properties, and one should be able to extract them without relying on measurements localized at an interface. This is critical in several situations where edges are difficult to probe, e.g., in disordered lattices [8,9]. Extracting topological invariants from the bulk is a challenging task in solid-state crystals.

Hence, artificial materials, e.g., arrays of cold atoms [10,11] or photonic crystals [12–14], are particularly appealing as they allow accessing topological properties of band structures through optical means [15–20].

In this work, we propose and experimentally demonstrate a powerful technique that allows measuring topological invariants in 2D artificial lattices with chiral symmetry. This technique, based on the concept of mean chiral displacement [21,22], consists in optically probing the spatial distribution of a wave packet for a specific momentum component. The experimental implementation of this scheme is realized in patterned semiconductor microcavities confining exciton polaritons [23]. This system is particularly well suited for this purpose, as its dissipative nature allows accessing both momentum and real-space profiles of Bloch modes with simple imaging techniques. Using polaritonic lattices emulating regular [24] and critically compressed [25] graphene (i.e., where Dirac cones have merged), we measure these 1D topological invariants and thus provide a direct evidence of the bulk-edge correspondence in these systems.

In the sublattice basis, the tight-binding Hamiltonian in momentum space describing a particle hopping on a honeycomb lattice is given by

$$H_{\text{HC}}(\vec{k}) = - \begin{pmatrix} 0 & g(\vec{k}) \\ g(\vec{k})^\dagger & 0 \end{pmatrix}, \quad (1)$$

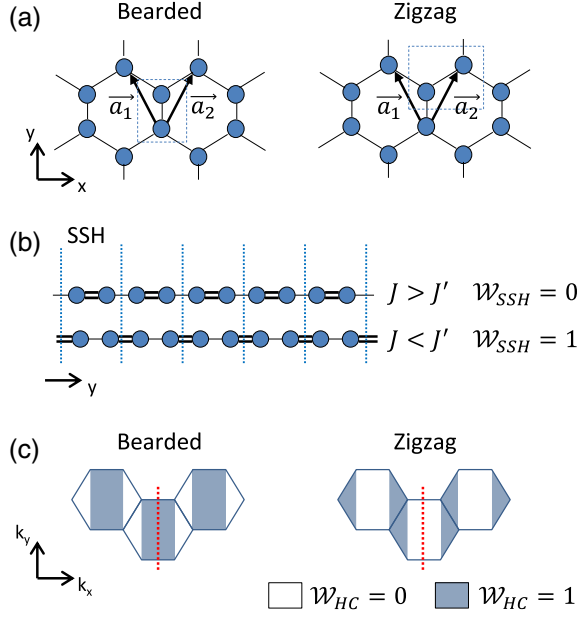


FIG. 1. (a) Definition of the unit cell for bearded and zigzag terminations. $\mathbf{a}_{1,2} = \{\pm 3/\sqrt{2}, 3/2\}a$ are the primitive vectors. (b) Schematic representation of the two topological phases of the SSH model. The dotted lines indicate the boundaries of unit cells. (c) Evolution of the winding number in graphene as k_x spans the BZ for bearded and zigzag terminations. White and blue regions correspond, respectively, to $\mathcal{W}_{HC} = 0$ and $\mathcal{W}_{HC} = 1$. Red dashed line indicates the position of $k_x = 0$.

where $g(\vec{k}) = j(1 + e^{-i\vec{k}\cdot\vec{a}_1} + e^{-i\vec{k}\cdot\vec{a}_2})$, with j the nearest-neighbor hopping amplitude. H_{HC} is defined for a unit cell compatible with bearded edges when considering a finite-sized ribbon along y , with periodic boundary conditions along x , see Fig. 1(a); for zigzag edges, $g(\vec{k}) = j(1 + e^{-i\vec{k}\cdot\vec{a}_2} + e^{i\vec{k}\cdot(\vec{a}_1 - \vec{a}_2)})$. For simplicity, we only consider bearded and zigzag terminations, but the argument and experimental technique developed in this work can be extended to arbitrary edges (such as armchair ones) [5].

The topological properties of this Hamiltonian are linked to its chiral symmetry associated to the anticommutation rule $\{H, \sigma_z\} = 0$, where σ_z is a Pauli matrix. This allows defining 1D topological invariants for each cut in the BZ along y . This is best seen by separating the momentum components parallel (k_x) and perpendicular (k_y) to the edge in $g(\vec{k})$:

$$g(\vec{k}) = J(k_x) + J'(k_x)e^{-i(3/2)ak_y}, \quad (2)$$

where $J(k_x) = \tilde{j}$ and $J'(k_x) = 2\tilde{j}\cos(\sqrt{3}ak_x/2)$ for bearded edges (with $\tilde{j} = je^{-i(\sqrt{3}ak_x/2)}$), and vice versa for zigzag edges. For each momentum component k_x , H_{HC} is isomorphic (along y) to the Hamiltonian of the well-known Su-Schrieffer-Heeger (SSH) model, which represents a 1D dimer chain with different intracell (J) and intercell (J') coupling energies [see Fig. 1(b)]. For this Hamiltonian, it is

possible to define a topological invariant called the winding number \mathcal{W}_{SSH} , which is equal to 0 for $|J/J'| > 1$ and equal to 1 for $|J/J'| < 1$. In the latter case, the nonzero topological invariant is linked to the existence of zero-energy edge states.

In a similar manner, it is possible to define a winding number of H_{HC} for each value of k_x :

$$\mathcal{W}_{HC}(k_x) = \frac{1}{2\pi} \int_{\text{BZ}} dk_y \frac{\partial \phi(\vec{k})}{\partial k_y}, \quad (3)$$

where $\phi(\vec{k}) = \arg[g(\vec{k})]$. This 1D topological invariant is equal to the geometric (or Zak) phase picked up by a particle spanning the BZ along k_y , divided by π . It can only take two values: 0 for $|J'(k_x)/J(k_x)| < 1$ and 1 for $|J'(k_x)/J(k_x)| > 1$ [see Fig. 1(c)], which is equal to the number of edge states at the corresponding momentum k_x [5–7,26]. Transitions from one value of the winding number to the other occur at the positions of the Dirac cones: this reflects the fact that the gap needs to close and reopen in order to change a topological invariant. Interestingly, for armchair terminations the winding number vanishes throughout the BZ because $g(\vec{k})$ always follows a straight line in the complex plane when k_x is varied.

The winding number of 1D chiral Hamiltonians can be extracted by probing the spatial evolution of a wave packet initially localized on a single unit cell [21,22] and computing a quantity called the mean chiral displacement. Related studies showed that the winding can also be extracted by preparing initial conditions on a single site of a given sublattice and measuring the mean displacement on the other sublattice only [8,27–29]. Hereafter, we demonstrate how this concept can be extended to two-dimensional lattices. This is realized in a hexagonal lattice of coupled micropillars obtained by etching a semiconductor planar microcavity confining exciton polaritons [see Fig. 2(a) and Supplemental Material [30]]. The coupling of the ground state of each pillar gives rise to two bands emulating the π and π^* bands of graphene [see Fig. 2(b)]. Throughout this work, we consider polaritonic states in the low power linear regime.

Our technique for extracting the mean chiral displacement as a function of k_x relies on photoluminescence (PL) measurements with combined real- and momentum-space resolution. The excitation is provided by a nonresonant cw laser focused on a single pillar that generates an incoherent wave packet spanning both energy bands. We then measure its time-integrated emission profile along y , while filtering a well-defined momentum component along x . This is done using the optical imaging technique described in Fig. 2(c), where a cylindrical lens (CL) with a curvature along x is positioned at a focal distance of the Fourier plane (red dashed line) of collection lens L_1 . The CL alters light trajectory only along x , providing a Fourier transform of the

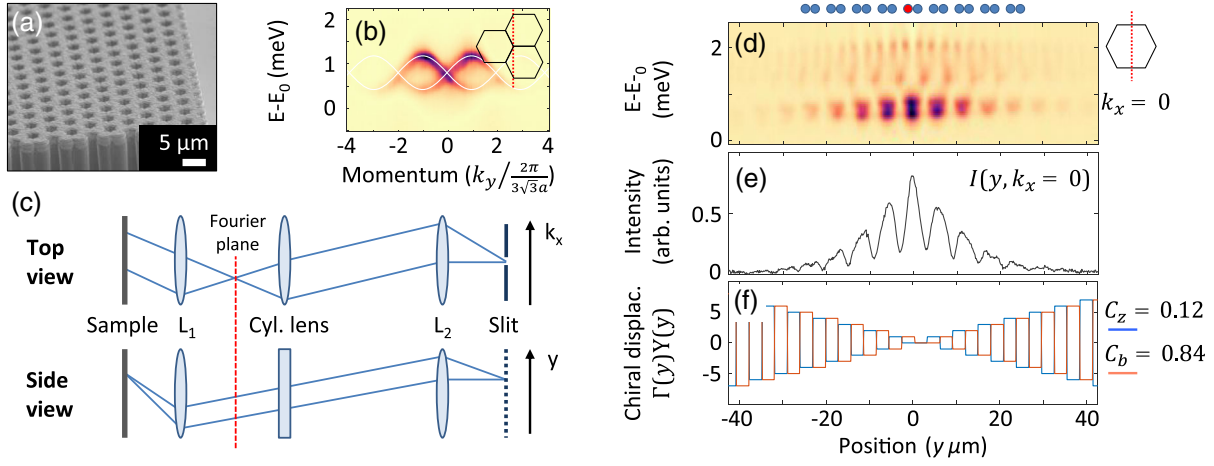


FIG. 2. (a) Scanning electron microscopy (SEM) image of a honeycomb lattice of coupled micropillars. (b) Momentum-resolved emission spectra of a polaritonic graphene lattice. $E_0 = 1.571$ eV. The cut in the BZ along which the image is taken is depicted in the inset. (c) Schematic representation of the setup. Upper and lower panels depict top and side views. (d) Spatially resolved steady-state emission spectra (along y) for a value of $k_x \sim 0$. The position of the different sites of the effective SSH lattice is indicated above, where the pumped pillar is in red. (e) Emission intensity integrated over both bands as a function of spatial position. (f) Definition of the chiral displacement ΓY as a function of spatial position. The blue (red) curves correspond to definition of the unit cell compatible with zigzag (bearded) edges. The values of the mean chiral displacements \mathcal{C}_z and \mathcal{C}_b extracted from the spectrum presented in (e) are given on the right-hand side of this panel.

emission in this direction (upper panel); along y , L_1 and L_2 simply provide real-space imaging of the emission (lower panel). Using a vertical slit at the imaging plane, this optical setup thus allows selecting a well-defined value of k_x , while simultaneously accessing the spatial profile along y .

Using this setup, Fig. 2(d) presents a spatially resolved (along y) emission profile for a position of the CL selecting momentum component $k_x \sim 0$. This steady-state emission profile clearly describes the physics of a dimer chain with a lower bonding band and an upper antibonding band. From this intensity profile, it is then possible to extract the winding number by computing the mean chiral displacement [21,22] (see Supplemental Material [30]):

$$\mathcal{C}(k_x) = \int dy 2\Gamma(y)Y(y)I^{(\text{int})}(y, k_x), \quad (4)$$

where the integral is taken over the entire emitting region. $I^{(\text{int})}(y, k_x)$ is the normalized energy-integrated spatial profile of the emission [Fig. 2(e)], $\Gamma(y)$ labels the sublattice index of the site [i.e., $+1$ (-1) for the A (B) sublattice], and $Y(y)$ labels the index of the unit cell (the wave packet is created in the zeroth unit cell). The product $\Gamma(y)Y(y)$ is a function describing the observable quantity associated to the chiral displacement operator $\hat{\Gamma} \hat{Y}$.

For a finite lattice, the unit cell is defined by the edge. However, in the bulk, the two definitions shown in Fig. 1(a) are equally valid, and, in the same experiment, we can compute \mathcal{W}_{HC} by simply shifting the definition of Γ . Values of $\Gamma(y)Y(y)$ are presented in Fig. 2(f), where the blue and red curves are compatible, respectively, with bearded and

zigzag terminations. Computation of the mean chiral displacement, for $k_x = 0$, leads to $\mathcal{C}_z = 0.12(8)$ and $\mathcal{C}_b = 0.84(8)$ for the zigzag and bearded edges, which clearly allows discriminating the two topological phases. The observed deviation from a quantized winding number is a direct consequence of the non-Hermitian nature of exciton polaritons: their finite lifetime prevents the wave packet from reaching a fully balanced distribution over the two sublattices (see Supplemental Material [30] for a derivation of \mathcal{C} in the presence of losses).

Note that the bands are not perfectly chiral symmetric, due to a slight deviation from the tight-binding approximation [31]. However, this asymmetry does not affect the measurement of the mean chiral displacement [30,32].

It is then possible to access profiles associated to different k_x values by laterally shifting the CL. Figures 3(a) and 3(b) show spatially resolved emission spectra for different k_x (indicated on the right). These profiles are qualitatively very different from the one measured at $k_x = 0$ as the effective coupling ratio (J'/J) changes. The emission pattern in Fig. 3(a) exhibits bands which are almost flat, as one of the two coupling coefficients vanishes. In Fig. 3(b), J'/J is negative, leading to a reversal of the bonding and antibonding bands.

Figure 3(c) presents measured values of the mean chiral displacement as a function of k_x , obtained by scanning laterally the CL. Solid lines show numerical calculations of the mean chiral displacement including the effect of polariton lifetime (see Supplemental Material [30]). These measurements of the mean chiral displacement show good agreement with the predicted values of the winding

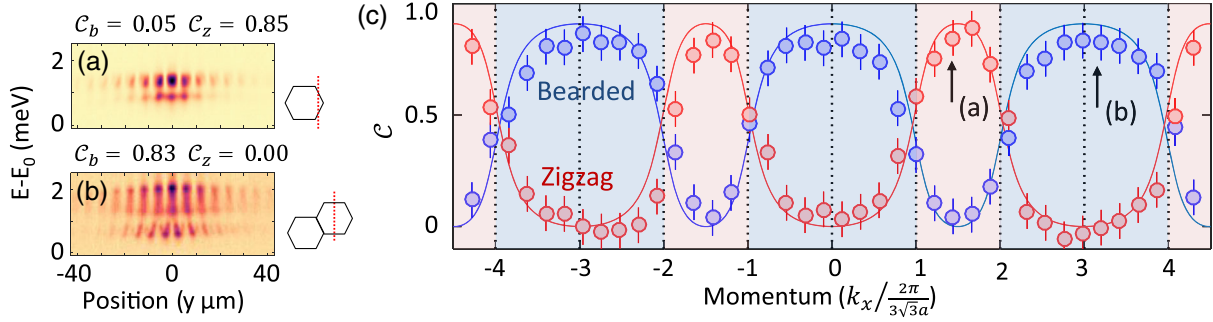


FIG. 3. (a),(b) Spatially resolved (along y) emission spectra for two distinct momentum components k_x schematically depicted on the right. Values of C for zigzag and bearded edges are provided above each panel. $E_0 = 1.571$ eV. (c) Evolution of the mean chiral displacement as a function of k_x . Blue and red circles correspond to values associated to the two possible definitions of the unit cell: respectively, bearded and zigzag. Blue (red) shaded areas correspond to regions where $\mathcal{W}_{\text{HC}} = 1$ for a unit cell definition compatible with zigzag (bearded) terminations. The solid line represents a theoretical calculation of the mean chiral displacement including losses, which is presented (along with error analysis) in Supplemental Material [30].

number: each time k_x crosses Dirac cones (indicated by vertical dotted lines), the values of C associated to each definition of the unit cell are exchanged, indicating a topological phase transition. Despite the presence of dissipation, these measured values of the mean chiral displacement present a clear contrast between high and low values, allowing us to unambiguously identify each topological phase. One important consequence of these transitions is the emergence (or disappearance) of zero-energy edge states as a function of k_x . Shaded blue (red) areas are indeed fully compatible with the values of k_x where zigzag (bearded) terminations exhibit edge states, as reported experimentally in Refs. [6,7,30].

Having demonstrated the measurement of winding numbers in a honeycomb lattice using the mean chiral displacement, we now show its versatility by applying this technique to a lattice compressed beyond the merging transition [33] of Dirac cones. It was shown, both theoretically [34,35] and experimentally [36–40], that applying a uniaxial strain to honeycomb lattices along the y axis by increasing the hopping amplitude j' with respect to j , as depicted in Fig. 4(a), shifts the position of the Dirac cones in the band structure along k_x . For strain coefficients $\beta = j'/j > 1$ (i.e., compression), K and K' Dirac cones move toward each other and merge at the critical value of $\beta = 2$, leading to the opening of an energy gap for every k_x . This disappearance of gap closings eliminates the previously observed topological transitions between regions separated by Dirac cones.

To demonstrate this disappearance of phase transitions, we fabricate a lattice of coupled micropillars with center-to-center distances $a = 2.4 \mu\text{m}$ and $a' = 1.7 \mu\text{m}$ corresponding to $\beta = 3$ [a SEM image of the lattice is shown in Fig. 4(b)]. Using the same measurement protocol as the one used for regular graphene, Fig. 4(c) presents the evolution of the values of mean chiral displacement as a function of k_x , for unit cells compatible with zigzag and bearded terminations. Both values of the mean chiral displacement

($C_b \sim 0.1$ and $C_z \sim 0.9$, respectively) are now independent of k_x , indicating the disappearance of topological phase transitions.

As a result, bearded terminations never present edge states, and zigzag ones do for all values of k_x . This is

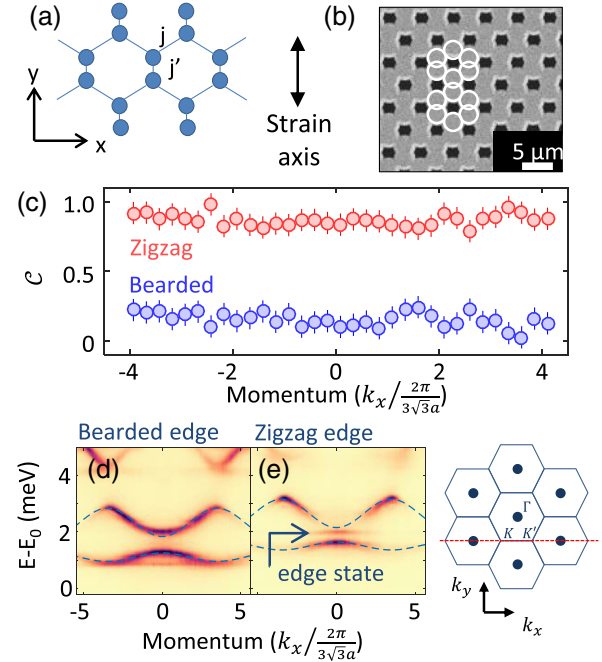


FIG. 4. (a) Schematic representation of the effect of compression on the lattice. The compression factor is defined as $\beta = j'/j$. (b) Top view SEM image of the compressed honeycomb lattice. White circles are added to indicate the positions of the pillars. (c) Evolution of the mean chiral displacement for both definitions of the unit cell. Blue circles correspond to the definition depicted in Fig. 1(a). (d),(e) Momentum-resolved PL spectra measured at the boundary of the lattice, along a bearded (d) and a zigzag (e) termination. The cut in the BZ along which both images are taken is depicted on the right. The blue arrow highlights the presence of an edge state in the zigzag termination case.

confirmed by probing the emission near the boundaries of the lattice: Figures 4(d) and 4(e) present PL spectra as a function of momentum along bearded and zigzag terminations, respectively. For the zigzag termination, an edge state band emerges in the center of the gap, whereas no edge state is observed for the bearded termination. This provides a direct evidence of the bulk-edge correspondence in this lattice.

In conclusion, we demonstrated a powerful approach for measuring 1D topological invariants from the bulk of 2D lattices presenting chiral symmetry. One important next step is to extend our scheme to more complex systems, e.g., involving flatbands [41,42], higher-energy orbitals [25,43], critical strain [40], or synthetic dimensions [44]. Furthermore, it would be interesting to explore how this scheme could be extended to the extraction of higher-order topological invariants [45–48] or Chern numbers in lattices with broken time-reversal symmetry [16]. Finally, although the present work deals with polaritons in the linear regime, their hybrid light-matter nature could allow probing, at higher excitation powers, the effect of interactions on topological invariants [49].

The authors acknowledge G. Montambaux for fruitful discussions. This work was supported by the H2020-FETFLAG project PhoQus (820392), the QUANTERA project Interpol (ANR-QUAN-0003-05), European Research Council (ERC) under the European Unions Horizon 2020 research and innovation programme (Grant Agreement No. 865151), the French National Research Agency project Quantum Fluids of Light (ANR-16-CE30-0021), the French government through the Programme Investissement d’Avenir (I-SITE ULNE/ANR-16-IDEX-0004 ULNE) managed by the Agence Nationale de la Recherche, the French RENATECH network, the Labex CEMPI (ANR-11-LABX-0007), the CPER Photonics for Society P4S and the Métropole Européenne de Lille (MEL) via the project TFlight. A. D. and P. M. acknowledge financial support from the Spanish Ministry MINECO (National Plan Grants FISICATEAMO No. FIS2016-79508-P, FIDEUA PID2019-106901GB-I00/10.13039/501100011033, and No. FIS2017-84114-C2-1-P, SEVERO OCHOA No. CEX2019-000910-S, FPI), European Social Fund, Fundació Cellex, Generalitat de Catalunya (AGAUR Grant No. 2017 SGR1341 and CERCA Program), ERC AdG NOQIA, MINECO-EU QUANTERA MAQS (funded by State Research Agency (AEI) PCI2019-111828-2/10.13039/501100011033), EU Horizon 2020 FET-OPEN OPTologic (Grant No 899794), the National Science Centre, Poland-Symfonia Grant No. 2016/20/W/ST4/00314, the “Juan de la Cierva” fellowship (IJCI-2017-33180), “Ramón y Cajal” program, and EU FEDER QuantumCAT _U16-011424, co-funded by ERDF Operational Program of Catalonia. P. S.-J. acknowledges financial support from the Marie Skłodowska-Curie

individual fellowship ToPol. A. D. acknowledges the financial support from a fellowship granted by la Caixa Foundation (Fellowship Code No. LCF/BQ/PR20/11770012).

-
- [1] M. Z. Hasan and C. L. Kane, Colloquium: Topological insulators, *Rev. Mod. Phys.* **82**, 3045 (2010).
 - [2] X. L. Qi and S. C. Zhang, Topological insulators and superconductors, *Rev. Mod. Phys.* **83**, 1057 (2011).
 - [3] D. J. Thouless, M. Kohmoto, M. P. Nightingale, and M. den Nijs, Quantized Hall Conductance in a Two-Dimensional Periodic Potential, *Phys. Rev. Lett.* **49**, 405 (1982).
 - [4] S. Ryu and Y. Hatsugai, Topological Origin of Zero-Energy Edge States in Particle-Hole Symmetric Systems, *Phys. Rev. Lett.* **89**, 077002 (2002).
 - [5] P. Delplace, D. Ullmo, and G. Montambaux, Zak phase and the existence of edge states in graphene, *Phys. Rev. B* **84**, 195452 (2011).
 - [6] Y. Plotnik, M. C. Rechtsman, D. Song, M. Heinrich, J. M. Zeuner, S. Nolte, Y. Lumer, N. Malkova, J. Xu, A. Szameit, Z. Chen, and M. Segev, Observation of unconventional edge states in ‘photonic graphene’, *Nat. Mater.* **13**, 57 (2014).
 - [7] M. Milićević, T. Ozawa, P. Andreakou, I. Carusotto, T. Jacqmin, E. Galopin, A. Lemaître, L. Le Gratiet, I. Sagnes, J. Bloch, and A. Amo, Edge states in polariton honeycomb lattices, *2D Mater.* **2**, 034012 (2015).
 - [8] E. J. Meier, F. Alex An, A. Dauphin, M. Maffei, P. Massignan, T. L. Hughes, and B. Gadway, Observation of the topological Anderson insulator in disordered atomic wires, *Science* **362**, 929 (2018).
 - [9] S. Stützer, Y. Plotnik, Y. Lumer, P. Titum, N. H. Lindner, M. Segev, M. C. Rechtsman, and A. Szameit, Photonic topological Anderson insulators, *Nature (London)* **560**, 461 (2018).
 - [10] N. Goldman, J. C. Budich, and P. Zoller, Topological quantum matter with ultracold gases in optical lattices, *Nat. Phys.* **12**, 639 (2016).
 - [11] N. R. Cooper, J. Dalibard, and I. B. Spielman, Topological bands for ultracold atoms, *Rev. Mod. Phys.* **91**, 015005 (2019).
 - [12] L. Lu, J. D. Joannopoulos, and M. Soljačić, Topological photonics, *Nat. Photonics* **8**, 821 (2014).
 - [13] T. Ozawa, H. M. Price, A. Amo, N. Goldman, M. Hafezi, L. Lu, M. C. Rechtsman, D. Schuster, J. Simon, O. Zilberberg, and I. Carusotto, Topological photonics, *Rev. Mod. Phys.* **91**, 015006 (2019).
 - [14] S. Klemmt, T. H. Harder, O. A. Egorov, K. Winkler, R. Ge, M. A. Bandres, M. Emmerling, L. Worschech, T. C. H. Liew, M. Segev, C. Schneider, and S. Höfling, Exciton-polariton topological insulator, *Nature (London)* **562**, 552 (2018).
 - [15] M. Atala, M. Aidelsburger, J. T. Barreiro, D. Abanin, T. Kitagawa, E. Demler, and I. Bloch, Direct measurement of the Zak phase in topological Bloch bands, *Nat. Phys.* **9**, 795 (2013).
 - [16] M. Aidelsburger, M. Lohse, C. Schweizer, M. Atala, J. T. Barreiro, S. Nascimbène, N. R. Cooper, I. Bloch, and N. Goldman, Measuring the Chern number of Hofstadter

- bands with ultracold bosonic atoms, *Nat. Phys.* **11**, 162 (2015).
- [17] L. Duca, T. Li, M. Reitter, I. Bloch, M. Schleier-Smith, and U. Schneider, An Aharonov-Bohm interferometer for determining Bloch band topology, *Science* **347**, 288 (2015).
- [18] N. Fläschner, B. S. Rem, M. Tarnowski, D. Vogel, D. S. Lühmann, K. Sengstock, and C. Weitenberg, Experimental reconstruction of the Berry curvature in a Floquet Bloch band, *Science* **352**, 1091 (2016).
- [19] M. Wimmer, H. M. Price, I. Carusotto, and U. Peschel, Experimental measurement of the Berry curvature from anomalous transport, *Nat. Phys.* **13**, 545 (2017).
- [20] A. Gianfrate, O. Bleu, L. Dominici, V. Ardizzone, M. De Giorgi, D. Ballarini, G. Lerario, K. W. West, L. N. Pfeiffer, D. D. Solnyshkov, D. Sanvitto, and G. Malpuech, Measurement of the quantum geometric tensor and of the anomalous Hall drift, *Nature (London)* **578**, 381 (2020).
- [21] F. Cardano, A. D'Errico, A. Dauphin, M. Maffei, B. Piccirillo, C. De Lisio, G. De Filippis, V. Cataudella, E. Santamato, L. Marrucci, M. Lewenstein, and P. Massignan, Detection of Zak phases and topological invariants in a chiral quantum walk of twisted photons, *Nat. Commun.* **8**, 15516 (2017).
- [22] M. Maffei, A. Dauphin, F. Cardano, M. Lewenstein, and P. Massignan, Topological characterization of chiral models through their long time dynamics, *New J. Phys.* **20**, 013023 (2018).
- [23] I. Carusotto and C. Ciuti, Quantum fluids of light, *Rev. Mod. Phys.* **85**, 299 (2013).
- [24] T. Jacqmin, I. Carusotto, I. Sagnes, M. Abbarchi, D. D. Solnyshkov, G. Malpuech, E. Galopin, A. Lemaître, J. Bloch, and A. Amo, Direct Observation of Dirac Cones and a Flatband in a Honeycomb Lattice for Polaritons, *Phys. Rev. Lett.* **112**, 116402 (2014).
- [25] M. Milićević, G. Montambaux, T. Ozawa, O. Jamadi, B. Real, I. Sagnes, A. Lemaître, L. Le Gratiet, A. Harouri, J. Bloch, and A. Amo, Type-III and Tilted Dirac Cones Emerging from Flat Bands in Photonic Orbital Graphene, *Phys. Rev. X* **9**, 031010 (2019).
- [26] K. Nakada, M. Fujita, G. Dresselhaus, and M. S. Dresselhaus, Edge state in graphene ribbons: Nanometer size effect and edge shape dependence, *Phys. Rev. B* **54**, 17954 (1996).
- [27] J. Cserti and G. Dávid, Relation between Zitterbewegung and the charge conductivity, Berry curvature, and the Chern number of multiband systems, *Phys. Rev. B* **82**, 201405(R) (2010).
- [28] J. M. Zeuner, M. C. Rechtsman, Y. Plotnik, Y. Lumer, S. Nolte, M. S. Rudner, M. Segev, and A. Szameit, Observation of a Topological Transition in the Bulk of a Non-Hermitian System, *Phys. Rev. Lett.* **115**, 040402 (2015).
- [29] Y. Wang, Y. Heng Lu, F. Mei, J. Gao, Z. Ming Li, H. Tang, S. Liang Zhu, S. Jia, and X. Min Jin, Direct Observation of Topology from Single-Photon Dynamics, *Phys. Rev. Lett.* **122**, 193903 (2019).
- [30] See Supplemental Material at <http://link.aps.org/supplemental/10.1103/PhysRevLett.126.127403>, which contains experimental details on the sample, the setup, the error analysis, complementary measurements on a 1D lattice, and theoretical sections detailing the calculation of the time-integrated mean chiral displacement with and without losses, which includes Refs. [21,22,31–32].
- [31] F. Mangussi, M. Milićević, I. Sagnes, L. Le Gratiet, A. Harouri, A. Lemaître, J. Bloch, A. Amo, and G. Usaj, Multi-orbital tight binding model for cavity-polariton lattices, *J. Phys. Condens. Matter* **32**, 315402 (2020).
- [32] S. Longhi, Probing one-dimensional topological phases in waveguide lattices with broken chiral symmetry, *Opt. Lett.* **43**, 4639 (2018).
- [33] A. D'Errico, F. Di Colandrea, R. Barboza, A. Dauphin, M. Lewenstein, P. Massignan, L. Marrucci, and F. Cardano, Bulk detection of time-dependent topological transitions in quenched chiral models, *Phys. Rev. Research* **2**, 023119 (2020).
- [34] B. Wunsch, F. Guinea, and F. Sols, Dirac-point engineering and topological phase transitions in honeycomb optical lattices, *New J. Phys.* **10**, 103027 (2008).
- [35] G. Montambaux, F. Piéchon, J. N. Fuchs, and M. O. Goerbig, Merging of Dirac points in a two-dimensional crystal, *Phys. Rev. B* **80**, 153412 (2009).
- [36] L. Tarruell, D. Greif, T. Uehlinger, G. Jotzu, and T. Esslinger, Creating, moving and merging Dirac points with a Fermi gas in a tunable honeycomb lattice, *Nature (London)* **483**, 302 (2012).
- [37] M. C. Rechtsman, Y. Plotnik, J. M. Zeuner, D. Song, Z. Chen, A. Szameit, and M. Segev, Topological Creation and Destruction of Edge States in Photonic Graphene, *Phys. Rev. Lett.* **111**, 103901 (2013).
- [38] M. Bellec, U. Kuhl, G. Montambaux, and F. Mortessagne, Topological Transition of Dirac Points in a Microwave Experiment, *Phys. Rev. Lett.* **110**, 033902 (2013).
- [39] M. Bellec, U. Kuhl, G. Montambaux, and F. Mortessagne, Manipulation of edge states in microwave artificial graphene, *New J. Phys.* **16**, 113023 (2014).
- [40] B. Real, O. Jamadi, M. Milićević, N. Pernet, P. St-Jean, T. Ozawa, G. Montambaux, I. Sagnes, A. Lemaître, L. Le Gratiet, A. Harouri, S. Ravets, J. Bloch, and A. Amo, Semi-Dirac Transport and Anisotropic Localization in Polariton Honeycomb Lattices, *Phys. Rev. Lett.* **125**, 186601 (2020).
- [41] W. Jiang, M. Kang, H. Huang, H. Xu, T. Low, and F. Liu, Topological band evolution between Lieb and kagome lattices, *Phys. Rev. B* **99**, 125131 (2019).
- [42] L.-K. Lim, J.-N. Fuchs, F. Piéchon, and G. Montambaux, Dirac points emerging from flat bands in Lieb-kagome lattices, *Phys. Rev. B* **101**, 045131 (2020).
- [43] M. Milićević, T. Ozawa, G. Montambaux, I. Carusotto, E. Galopin, A. Lemaître, L. Le Gratiet, I. Sagnes, J. Bloch, and A. Amo, Orbital Edge States in a Photonic Honeycomb Lattice, *Phys. Rev. Lett.* **118**, 107403 (2017).
- [44] T. Ozawa and H. M. Price, Topological quantum matter in synthetic dimensions, *Nat. Rev. Phys.* **1**, 349 (2019).
- [45] C. W. Peterson, W. A. Benalcazar, T. L. Hughes, and G. Bahl, A quantized microwave quadrupole insulator with topologically protected corner states, *Nature (London)* **555**, 346 (2018).
- [46] M. Serra-Garcia, V. Peri, R. Süsstrunk, O. R. Bilal, T. Larsen, L. Guillermo Villanueva, and S. D. Huber, Observation of a phononic quadrupole topological insulator, *Nature (London)* **555**, 342 (2018).

- [47] S. Mittal, V. Vikram Orre, G. Zhu, M. A. Gorlach, A. Poddubny, and M. Hafezi, Photonic quadrupole topological phases, *Nat. Photonics* **13**, 692 (2019).
- [48] A. El Hassan, F. K. Kunst, A. Moritz, G. Andler, E. J. Bergholtz, and M. Bourennane, Corner states of light in photonic waveguides, *Nat. Photonics* **13**, 697 (2019).
- [49] S. De Léséleuc, V. Lienhard, P. Scholl, D. Barredo, S. Weber, N. Lang, H. Peter Büchler, T. Lahaye, and A. Browaeys, Observation of a symmetry-protected topological phase of interacting bosons with Rydberg atoms, *Science* **365**, 775 (2019).